Energy & Environmental Science

ROYAL SOCIETY OF CHEMISTRY

PAPER

View Article Online
View Journal | View Issue

Check for updates

Cite this: *Energy Environ. Sci.*, 2023, **16**, 2945

# Surface crystallinity enhancement in organic solar cells induced by spinodal demixing of acceptors and additives†

Zichao Shen,[ab] Jinde Yu,*[ab] Guanyu Lu,[a] Keming Wu,[c] Qingyu Wang,[ab] Laju Bu,[ab] Xinfeng Liu,[c] Yuanwei Zhu*[ab] and Guanghao Lu*[ab]

Although non-volatile additives like 1,8-diiodooctane (DIO) and 1-chloronaphthalene (CN) are beneficial for improving the power conversion efficiency (PCE) of organic solar cells (OSCs), the effects of such additives on phase evolution are still ambiguous. Here the phase evolution of the representative systems PBDB-T:ITIC (including ITIC's derivatives) and PM6:Y6 with DIO/CN additives is investigated by a combination of position-resolved and time-resolved spectroscopy techniques, namely film-depth-dependent light absorption spectroscopy (FLAS) and time-dependent light reflection/scattering/fluorescence spectroscopy. It is found that during solvent evaporation, a solvent-free liquid film surface (additive-enriched) is formed owing to the volatility difference between chlorobenzene/chloroform (CB/CF) and DIO/CN. Consequently, the Flory–Huggins interaction parameters are calculated. For the DIO:ITIC binary surface, if the donor is absent, spinodal demixing produces highly ordered crystals compared to the crystals inside the film, while for the CN:Y6 surface, binodal demixing occurs as in the liquid film bulk. Ultraviolet photoelectron spectroscopy (UPS) and low-energy inverse photoemission spectroscopy (LEIPS) results show that the surface of PBDB-T:ITIC with 0.5% DIO features highly ordered crystalline ITIC with the energy levels (HOMO and LUMO) rising as much as 0.42 eV, leading to poor charge transport properties. After thermal annealing (TA), the partial ITIC on the surface transforms to an edge-on orientation owing to Ostwald ripening, leading to a decrease of ITIC's energy level by 0.81 eV, which matches that of PBDB-T. In contrast, the surface absorption spectra of PM6:Y6 blend films deposited with 0.5% CN are invariable after TA treatment, contributing to less PCE variation. The performances of additive devices with different TA conditions are associated with the optical absorption of the film surface, proving that surface phase segregation significantly determines the photovoltaic performance.

Received 9th January 2023,
Accepted 14th April 2023

DOI: 10.1039/d3ee00090g

rsc.li/ees

Published on 08 May 2023. Downloaded by Xian Jiaotong University on 2/27/2026 2:24:49 AM.

## Broader context

Non-volatile additives like 1,8-diiodooctane (DIO) and 1-chloronaphthalene (1-CN) are commonly used for promoting the power conversion efficiency (PCE) of organic solar cells (OSCs) through morphology and crystallinity control; however, effort on the investigation of the working mechanism of such additives is limited. Herein, focusing on the surface phase evolution of liquid films, film-depth-dependent light absorption spectroscopy (FLAS) and time-dependent light reflection/scattering/fluorescence spectroscopy are employed for investigating the phase evolution of the representative systems PBDB-T:ITIC (including ITIC's derivatives) and PM6:Y6 with DIO/CN additives, verifying that the surface of the liquid film is solvent free. The surface spinodal demixing and binodal demixing for DIO:ITIC and CN:Y6, respectively, are consequently demonstrated using calculated Flory–Huggins interaction parameters. The spinodal demixing of DIO:ITIC leads to the formation of highly ordered ITIC surface domains, possessing unmatched energy levels with PBDB-T, thus resulting in poor electron mobility. In contrast, the CN:Y6 blend undergoes a binodal demixing process which is similar to that in the liquid film bulk, contributing to a uniform crystallinity distribution along the film-depth direction. After thermal annealing (TA), the partial ITIC on the surface transforms into an edge-on orientation owing to Ostwald ripening, leading to a decrease in ITIC's energy level by 0.81 eV, which matches that of PBDB-T. In contrast, the surface absorption of the PM6:Y6 blend film with 0.5% CN is invariable after TA treatment, contributing to less PCE variation. The surface phase segregation is proven to significantly determine the photovoltaic performance. This work readdresses the rationale for using additives and TA treatment, helping to improve the performances of OSCs and other organic electronics.

[a] *Frontier Institute of Science and Technology, and School of Chemistry, Xi'an Jiaotong University, Xi'an 710054, China. E-mail: guanghao.lu@mail.xjtu.edu.cn, doucomon@stu.xjtu.edu.cn, zhuyuanwei@xjtu.edu.cn*

[b] *State Key Laboratory of Electrical Insulation and Power Equipment, Xi'an Jiaotong University, Xi'an 710049, China*

[c] *CAS Key Lab Standardizat & Measurement Nanotechnol, Natl Ctr Nanosci & Technol, Beijing 100190, People's Republic of China*

† Electronic supplementary information (ESI) available. See DOI: https://doi.org/10.1039/d3ee00090g

Published on 08 May 2023. Downloaded by Xian Jiaotong University on 2/27/2026 2:24:49 AM.

## Introduction

Conjugated organic semiconductors possess advantages such as being cheap, solution processable, flexible, *etc.*, due to which they are now widely investigated in organic electronics such as organic field-effect transistors, organic light emitting diodes and organic solar cells (OSCs).[1–3] In OSCs, non-fullerene acceptors (NFAs) have replaced fullerene acceptors because they are more efficient.[4–7] Power conversion efficiency (PCE) is a decisive parameter characterizing the performance of OSCs, and is obtained by multiplying the open-circuit voltage ($V_{OC}$), the short-circuit current density ($J_{SC}$) and the fill factor (FF). The PCEs of fullerene-based OSCs are rarely over 10% while the PCEs of the NFA OSCs can easily achieve 10% by employing ITIC and its derivatives as acceptors.[8,9] Newly developed Y6 and its derivatives are the state-of-the-art NFAs which can achieve the PCEs over 18%.[10–13]

Although the research on the process of NFA OSCs is rapidly advancing, the method of solvent additives still has not been replaced.[14–16] The non-volatile solvent 1,8-diiodooctane (DIO) was introduced in solution in order to optimize the morphology of the small molecule acceptors,[17–21] *e.g.* PCBM and ITIC. For the most efficient device PM6:Y6, 1-chloronaphthalene (1-CN) is frequently employed as an effective additive, which is also a non-volatile solvent, having similar functions to DIO. Generally recognized principles are crystallinity enhancement with a non-volatile solvent added, which further leads to efficient exciton dissociation and optimized charge transport properties.[22–26] Although the solvent additive method is effective and still widely used today, the working mechanism has not been investigated thoroughly, especially from the viewpoint of film evolution and vertical morphology.[27–29] Furthermore, the additives like DIO can improve the film crystallinity and thus further affect the charge transport energy levels, which also has not been well understood. It is worth mentioning that the additives can sometimes deteriorate the device performance if the film deposition is not optimized, which is still not well explained.[30,31]

In addition, so far the methods for investigating the organic thin-film vertical morphology are rare and inconvenient, such as film-depth-dependent X-ray photoelectron spectroscopy and secondary ion mass spectroscopy, from which only a little information can be extracted and is mainly the vertical component distribution.[27,28] The FLAS technology was recently developed by us, which can efficiently analyze the film-depth dependent spectral morphology by etching the sample with soft plasma and *in situ* collecting its UV-vis absorption spectra synchronously.[32–36] Sub-layer crystallinity, film-depth dependent component distribution, and the exciton generation rate profile can be extracted from the FLAS results. The FLAS technology is usually employed in the fields of organic field-effect transistors, organic light emitting diodes and OSCs. Because the addition of additives in OSCs is aimed to improve the crystallinity of the active layer, using FLAS to study the effects of additives on OSCs is a very efficient method.

In this work, the FLAS technology supplemented by time-dependent light reflection spectroscopy and dynamic light scattering/fluorescence spectroscopy are employed to analyze the phase evolution and vertical morphology of PBDB-T:ITIC (including ITIC's derivatives) and PM6:Y6 blends affected by DIO/CN (here "DIO/CN" represents "DIO or CN") additives. The surface spinodal demixing and binodal demixing for DIO:ITIC and CN:Y6 (here "DIO:ITIC" represents "DIO and ITIC blends"), respectively, are demonstrated by calculated Flory–Huggins interaction parameters. The spinodal demixing of DIO:ITIC leads to the formation of highly ordered ITIC surface domains, possessing unmatched energy levels with PBDB-T, thus resulting in poor electron mobility. In contrast, the CN:Y6 blend undergoes a binodal demixing process at the surface, which is similar to the scenario in the liquid bulk, contributing to a uniform crystallinity distribution along the film-depth direction. The surface phase segregation significantly determines the photovoltaic performance. This work readdresses the rationale for using additives and thermal annealing (TA) treatment, helping to improve the performances of OSCs and other organic electronics.

## Results and discussion

### Surface absorption characterization *via* the FLAS method

We chose PBDB-T:ITIC (including ITIC's derivatives) and PM6:Y6 devices with 0.5% DIO/CN additives as examples to study the additive effect because both Y6 and ITIC are very efficient and characteristic NFAs in the OSC field (Fig. 1(a)).[37,38] We fabricated PBDB-T:ITIC and PM6:Y6 devices with different treatments (with or without additives; with or without TA), and FLAS measurement was carried out in order to investigate the impact of additives on vertical phase segregation (Fig. S1, ESI†). As we can see, only for the 1st sub-layer (top surface), the ITIC absorption peak is significantly different from that of the PBDBT:ITIC film without TA treatment. For PM6:Y6 blend films, the FLAS results of different treatments are almost identical. For the PBDB-T:ITIC blend film with 0.5% DIO addition, a sharp absorption peak of ITIC in the 1st sub-layer (surface) located at 710.6 nm is observed, and after TA treatment, this sharp peak becomes flatter in combination with a blue shift of around 20 nm, as shown in Fig. 1(b). This phenomenon is also observed in a 0.5% DIO added pure ITIC film, as shown in Fig. S2 (ESI†), which has not been reported and is beyond expectation. Generally, TA treatment is an Ostwald ripening process, which is able to help crystals to grow and age, so as a result, the absorption peaks should be red-shifted because of the reduced HOMO energy level.[39] The 1st sub-layer absorption of PM6:Y6 with 0.5% CN follows the general rule (Fig. 1(b)) and it is very similar to other sub-layers, representing higher regularity, which is beneficial for the device performance. We further compared the absorption spectra of the 1st sub-layer (0.5% DIO, without TA) of the ITIC neat film and the film deposited from the DIO solution (see Fig. 1(c)), and the results show that they are very similar. In that case, the 1st sub-layer seems to be formed from the DIO solution rather than the CB solution, and the property of this layer is naturally quite different. In contrast, the absorption

 This journal is © The Royal Society of Chemistry 2023

Published on 08 May 2023. Downloaded by Xian Jiaotong University on 2/27/2026 2:24:49 AM.

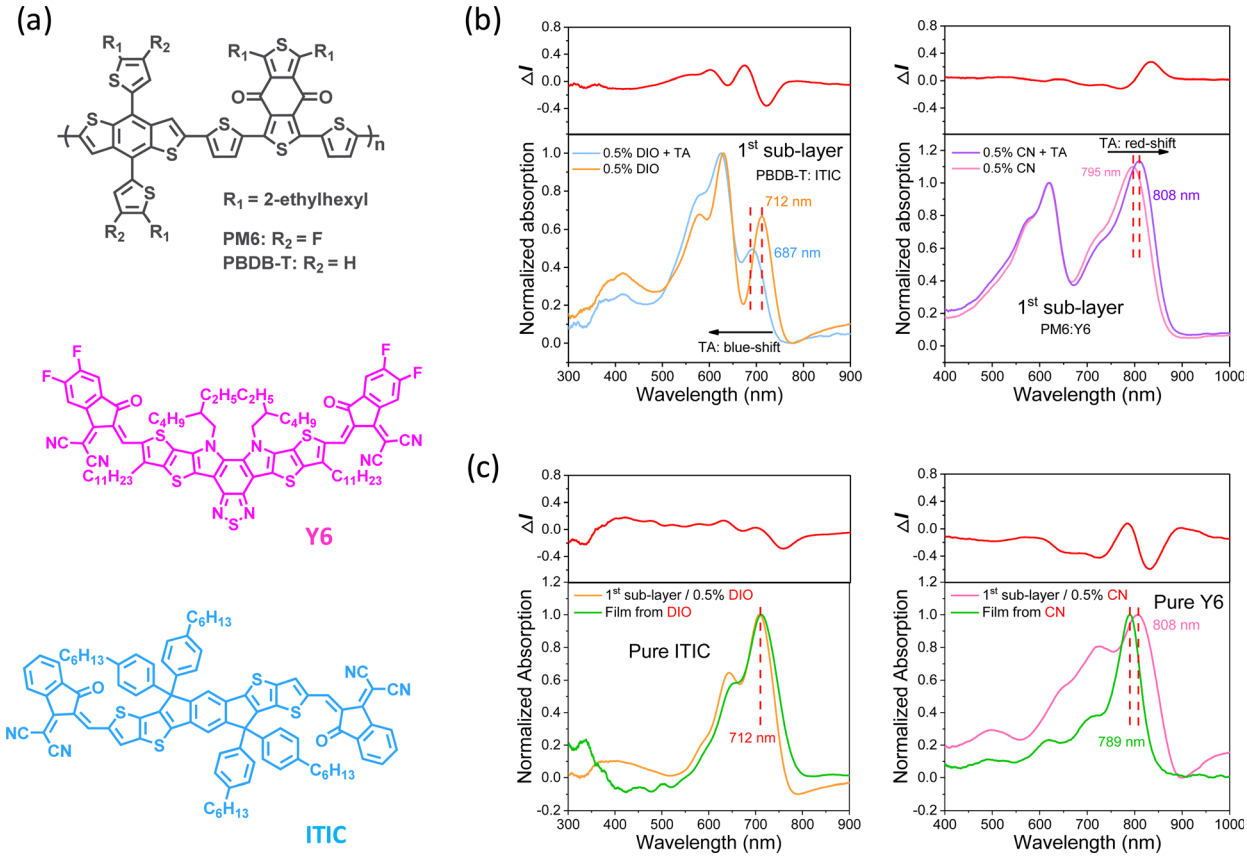



Fig. 1 UV-vis absorption spectra of PBDB-T:ITIC and PM6:Y6 blend films with different treatments (with or without DIO; with or without TA). (a) Molecular structures of PBDB-T, PM6, Y6 and ITIC. (b) Absorption differences of the 1st sub-layers of PBDB-T:ITIC and PM6:Y6 blend films with different treatments. After TA treatment, the absorption peak of ITIC is blue-shifted and becomes weaker, while the absorption peak of Y6 shows a slight red-shift. (c) Absorption spectra of PBDB-T:ITIC and PM6:Y6 blend films deposited from additives (as solvents) or additive-containing mixture solvents. The up-figures and down-figures in (b) and (c) share the same *x*-axis.

spectra of the 1st sub-layer (0.5% CN, without TA) of the Y6 neat film and the film deposited from CN solution show a very large variation, indicating that the 1st sub-layer is not formed from CN solution.

### Phase evolution characterization and surface liquid–solid transition calculations

ITIC's special surface absorption indicates a special film formation process. Time-dependent light reflection spectroscopy is employed for surface segregation measurement of PBDB-T:ITIC blend films (with or without DIO), and the results are provided in Fig. 2(a) and (b), in which PBDB-T precipitation is observed at the beginning of spin-coating, indicating that the liquid film surface is solvent free. Unlike the low boiling solvent CB (132 °C), DIO (332.5 °C) is much harder to evaporate.[40,41] Ideally speaking, DIO should exhibit equal distribution along the vertical direction. Below the surface, for the 0.5% DIO/CB solvent, the solution can be regarded as CB solution, while at the air–liquid interface, in the absence of the CB solvent, the surface can be regarded as the DIO solution. It is also understandable that the solvent molecules move from the surface to the air much more easily than from inside the solution to the surface, thus forming an approximate solvent free surface. Due to the substrate reflection (>700 nm), the reflection of ITIC cannot be observed, but ITIC must precipitate together with PBDB-T owing to the solvent free surface. Fig. 2(c) is the reflection measurement of the quartz covering test for the PBDB-T:ITIC liquid film. After quartz was covered, which is aimed to replace the air–liquid interface with the quartz–liquid interface, the characteristic reflection of PBDB-T vanished, well proving that the precipitated layer is on top of the liquid film.

Given the approximate solvent free surface, we can think of the liquid film surface as a binary system (because the absorption of the donors does not vary with film depth and after-treatment, the donors are not shown for clarity), which is composed of additives and acceptors, while the liquid film bulk is a ternary system composed of additives, acceptors and solvents.

For the liquid film bulk, binodal demixing is generally believed for phase separation, owing to the existence of the solvent. Time-dependent light scattering/fluorescence spectroscopy is employed for the detection of crystal nuclei. The result of time-dependent light scattering/fluorescence spectroscopy shown as a contour map is provided in Fig. 2(d), and the profile of scattering at 530 nm is provided in Fig. 2(e). As we can see, the scattering intensity keeps increasing in the time range of 0–6000 ms, while the solution fluorescence keeps decreasing,

Published on 08 May 2023. Downloaded by Xian Jiaotong University on 2/27/2026 2:24:49 AM.

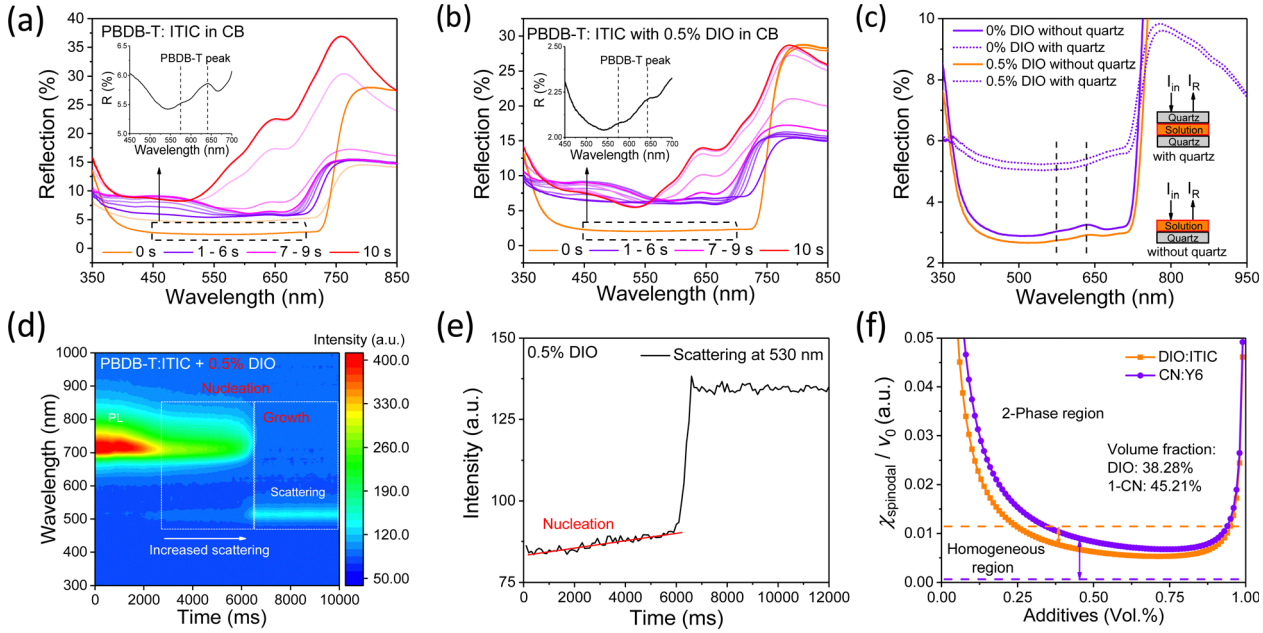



Fig. 2 Time-dependent spectral detection of surface precipitation and nucleation process of PBDB-T:ITIC in CB solution with or without 0.5% DIO addition. (a), (b) time-dependent light reflection spectra of PBDB-T:ITIC in CB with or without 0.5% DIO addition. (c) Reflection measurement of the quartz covering test for the PBDB-T:ITIC liquid film. The characteristic reflection of PBDB-T vanished after quartz was covered, meaning that the precipitated layer is on the top of the liquid film. (d) Contour of time-dependent light scattering of PBDB-T:ITIC blends with or without DIO. (e) Profiles of scattering at 530 nm. (f) The additives/acceptors liquid–solid transition diagrams estimated for DIO:ITIC and CN:Y6 as a function of the volume fraction of additives. The dashed lines represent the interaction parameters of additive–acceptor blends.

indicating that the crystal nuclei are growing larger. The nucleation and growth processes are representative phenomena of binodal demixing.[42,43]

For the liquid film surface, spinodal demixing is evidenced by the additives/acceptors liquid–solid phase transition diagrams estimated for PBDB-T:ITIC and PM6:Y6 as a function of the volume fraction of different additives.[44] The condition $\partial^2 \Delta G_{mix}/\partial \varphi^2 > 0$ is required and the value of spinodal interaction parameter $\chi_{spinodal}$ that determines the boundary between the homogenous region and two-phase region can be obtained by,

$$\chi_{spinodal} = \frac{\nu_0}{2}\left(\frac{\rho_1}{M_1\varphi_1} + \frac{\rho_2}{M_2(1-\varphi_1)}\right) \quad (1)$$

where $\nu_0$ is the molar volume of the lattice site in the Flory–Huggins model; $\rho_1$, $M_1$ and $\varphi_1$ are the density, molecular weight and fraction volume of additives, respectively; $\rho_2$ and $M_2$ are the density and the molecular weight of acceptors, respectively. From homogeneous Flory–Huggins solution theory (eqn (2)), the interaction parameters $\chi_{1,2}$ of DIO:ITIC and CN:Y6 can be empirically calculated as follows:

$$\chi_{1,2} = \frac{\nu_0}{RT}\left(\delta_{T_1} - \delta_{T_2}\right)^2 \quad (2)$$

where $\nu_0$ is the molar volume of the lattice site in the Flory–Huggins model, and $\delta_T$ is the Hildebrand solubility parameter.

Fig. 2(f) shows the additives/acceptors liquid–solid phase transition diagrams estimated for DIO:ITIC and CN:Y6 as a function of the volume fraction of additives. The $\chi_{spinodal}/\nu_0$ values are used for better comparison between different blend systems. The dashed lines represent the calculated interaction parameters $\chi_{1,2}/\nu_0$ of additive-acceptor blends, which are based on the values from the literature (see Table S1, ESI†).[45,46] The interaction parameters of DIO:ITIC, $\chi_{DIO,ITIC}/\nu_0$ = 0.0115, are located at the two-phase region with a DIO volume fraction of 38.28%, indicating that DIO and ITIC will separate through spinodal demixing, while the interaction parameter of CN:Y6, $\chi_{CN,Y6}/\nu_0$ = 0.0007, is located at the homogeneous region with a CN volume fraction of 45.21%, signifying that CN and Y6 will separate through binodal demixing. Large solubility parameter differences between DIO and ITIC lead to poor miscibility, which is the primary cause of surface spinodal demixing. The atomic force microscopy (AFM) results of ITIC films with different treatment conditions, which are provided in Fig. S3 (ESI†), show that the ITIC film with 0.5% DIO before TA-treatment possesses the largest surface roughness of 4.0 nm, manifesting the surface spinodal demixed highly ordered ITIC domain.

CN is also used as an additive for PBDB-T:ITIC blends and using DIO for PM6:Y6 blends. The FLAS results are provided in Fig. S4 (ESI†). As we can see, both ITIC and Y6 absorption peaks are not obviously shifted after TA treatment, which indicates that during solvent evaporation no spinodal demixing occurs at the liquid film surface of both PBDB-T:ITIC and PM6:Y6 films. The additives/acceptors liquid–solid transition diagrams of ITIC:CN and Y6:DIO are also shown in Fig. S5 (ESI†), and the results show that both $\chi_{DIO,Y6}/\nu_0$ and $\chi_{CN,ITIC}/\nu_0$ are located in the homogeneous region, indicating binodal demixing at the liquid film surface during the film formation process from solution.

 This journal is © The Royal Society of Chemistry 2023

Published on 08 May 2023. Downloaded by Xian Jiaotong University on 2/27/2026 2:24:49 AM.

According to the evidence summarized above, we consider differential surface-bulk phase evolution described as shown in Fig. 3. For simplicity, the donors have not been shown, because no significant absorption change of donors is observed in both PBDB-T:ITIC and PM6:Y6 films deposited with additives before and after TA treatment. The phase evolution can be divided into 5 steps, which are no. 1 stage, solution state. In this state, both the ITIC and Y6 solution surfaces are homogeneous, and the ITIC surface is in an unstable state; no. 2 stage, surface spinodal demixing. This step only takes place at the DIO:ITIC liquid film surface, owing to its poor miscibility, while the surface of the CN:Y6 liquid film and the ternary liquid bulk of both DIO:ITIC and CN:Y6 remain homogeneous; no. 3 stage, bulk nucleation (binodal demixing). With the evaporation of the solvent inside the liquid film, the liquid bulk of both DIO:ITIC and CN:Y6 starts to nucleate, and during this process, light scattering keeps increasing; no. 4 stage, dried films. After most solvent has evaporated, the film has almost dried, and the molecules in the dried film are frozen. The highly ordered ITIC spinodal demixed domain is located at the ITIC film surface, while the semi-crystalline binodal demixed domain lies inside the ITIC film. For the CN:Y6 film, the surface demixes through a binodal path together with the liquid film bulk. No. 5 stage, TA treatment. Given the Ostwald ripening, the highly ordered surface of the DIO:ITIC film vanishes, and ITIC molecules at the film surface are assimilated by the film bulk, forming a uniform crystallinity distribution along the film-depth direction. For the CN:Y6 film, TA treatment only helps to modify the crystal defects.

The schematic diagram of donor behaviours during the film formation process is provided in Fig. S6 (ESI†). The donor will also deposit at the liquid film surface together with the acceptors, according to the time-dependent light reflection spectroscopy results. However, the effect of additives on donor behaviours is weak because the donor is not able to be dissolved by the additives.

### Surface molecular structural characterization

In order to characterize the out-of-plain molecular orientation structure of the highly ordered surface, we carried out the

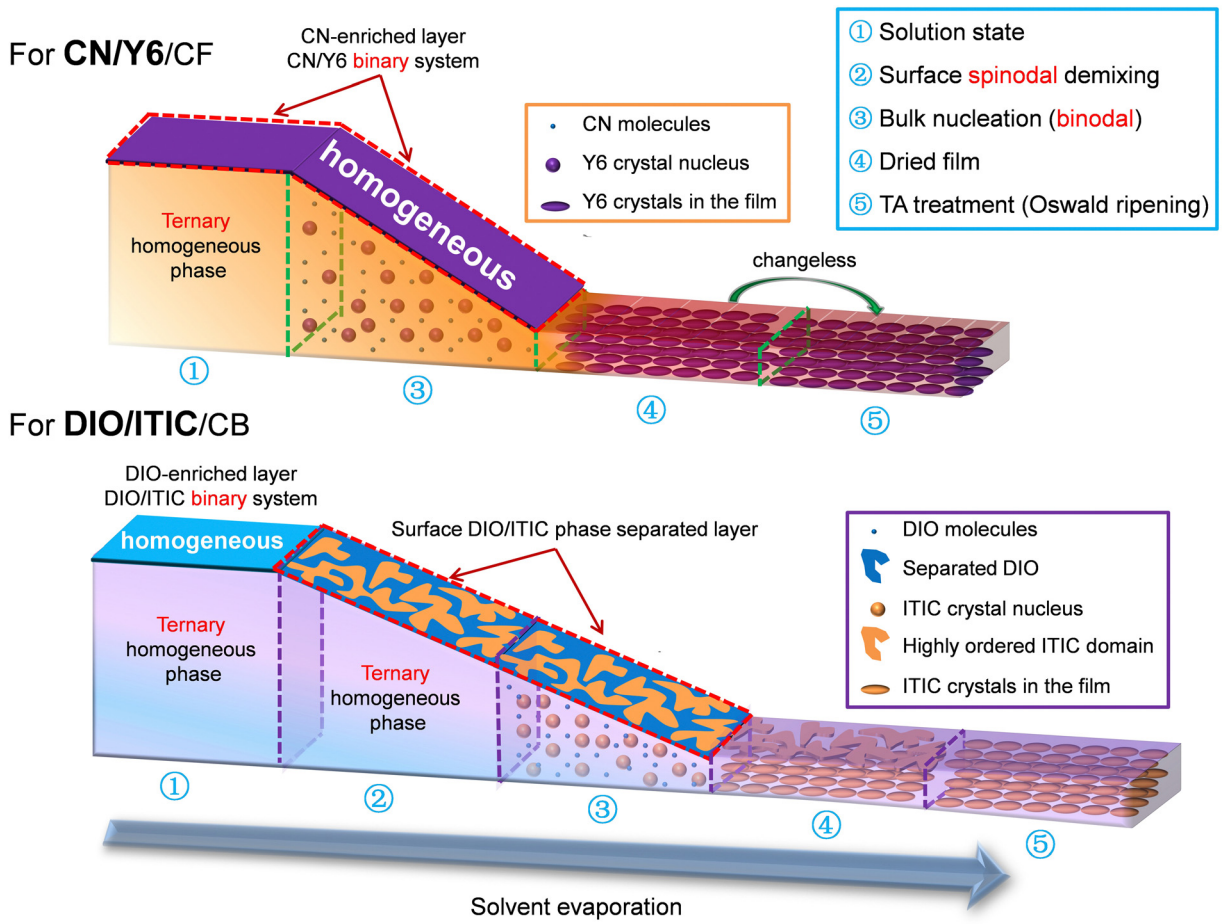



Fig. 3 Schematic diagram of film formation process with additive-enriched surfaces. For simplicity, the donors are not shown here. Given the solvent's fast evaporation, the surface of the liquid film can be regarded as an additive/acceptor binary system, while the bulk of the liquid film remains a ternary homogeneous phase. Unlike the homogeneous surface of CN/Y6 blends, the surface formed by the DIO/ITIC binary blend is an unstable system, and thus the phase separation of DIO and ITIC will occur *via* spinodal demixing. In contrast, the CN/Y6 surface and the acceptors in the liquid film bulk will crystallize *via* binodal demixing. The crystallinity of the spinodal-produced surface highly ordered ITIC domains would be degraded after TA treatment owing to Ostwald ripening.

Published on 08 May 2023. Downloaded by Xian Jiaotong University on 2/27/2026 2:24:49 AM.

angle-dependent near-edge X-ray absorption fine structure (NEXAFS) scans of ITIC and Y6 neat films with additives before and after TA treatment. As demonstrated in Fig. 4(a), angle-dependent NEXAFS scans are able to probe the angle-dependent K-shell electron C 1s-π* resonance, which determines the conjugated molecular backbone orientation, because the transition dipole moment (TDM) of the C 1s-π* resonance is orthogonal to the conjugated plane.[47] It is worth mentioning that polarized X-rays are more commonly employed for better characterization of the in-plain anisotropic system, while non-polarized X-rays are adequate for out-of-plain orientation determination. Unlike the grazing incident wide angle X-ray scattering (GIWAXS) measurement, which is bulk-sensitive if the incident angle is larger than the critical angle (~0.1°), the NEXAFS measurement is extremely surface-sensitive (<3 nm), which is more sufficient for probing the surface molecular backbone orientation.[48] As a matter of fact, even if the incident angle used in GIWAXS measurement is smaller than 0.1°, the penetrability of the X-ray beam is still as deep as 5–10 nm, which is too deep for the surface characterization. For the face-on backbone orientation, the C 1s-π* resonance will be stronger with the incident angle decreasing, while for the edge-on backbone orientation, the C 1s-π* resonance is supposed to be invariable with the incident angle. Fig. 4(b) and (c) demonstrate the angle-dependent NEXAFS results of Y6 and ITIC neat films, respectively. As we can see, the C 1s-π* resonances of all the conditions located at ~285 eV become stronger as the incident angle decreases, representing the dominant surface face-on orientation. Similar angle-dependent tendencies of Y6 films before and after TA treatment mean that the molecular orientation of Y6 at the surface does not change, while the resonance of ITIC drops slower after TA treatment, representing partial edge-on orientation transformation. The angle-dependent C 1s-π* resonance intensity $I_{(\theta)}$ (at 285 eV) can be described by the fit coefficients of a linear relationship,[49]

$$I_{(\theta)} = A + B\sin^2\theta \quad (3)$$

where $A$ and $B$ are fit coefficients. The slope $B$ is correlated with the degree of the face-on orientation, and the bigger absolute value of $B$ represents the higher degree of the face-on orientation. The slope $B$ values of Y6 films with 0.5% CN before and after TA treatment are −3.05 and −2.98, respectively, exhibiting no significant variation, while the slope $B$ values of ITIC films with 0.5% DIO before and after TA treatment are −3.23 and −1.94, representing a TA-dependent orientation. NEXFAS is averaged molecular orientation information with contribution by all molecules, and thus the lower $B$ value represents partial declination from a face-on orientation. The main function of TA treatment is to promote Ostwald ripening, illustrating that the surface highly ordered ITIC layer is absorbed by the underneath ITIC crystals after TA treatment, while the surface and bulk of Y6 films should possess a similar orientation and thus

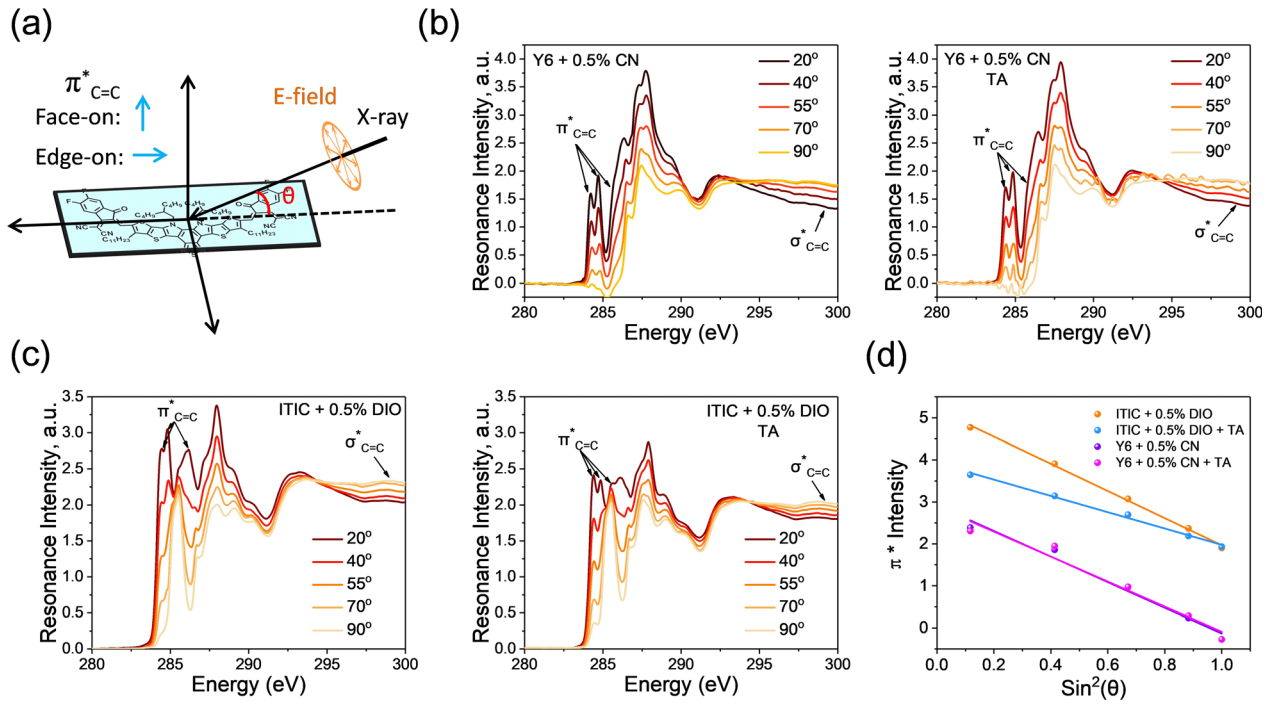



Fig. 4 Angle-dependent NEXAFS measurement results. (a) Illustration of NEXAFS measurements of Y6/ITIC with the incident angle $\theta$ using an X-ray beam. The transition dipole moment (TDM) of the C 1s-π* resonance is orthogonal to the conjugated plane, and thus if with the increase of the incident angle, the $\pi_{C=C}$* absorption is weakened, which means the molecules on the surface prefer a face-on orientation; otherwise they prefer an edge-on orientation. (b) Angle-dependent NEXAFS spectra of Y6 with 0.5% CN before and after TA treatment. The C 1s-π* resonances of Y6 with 0.5% CN before and after TA treatment are almost the same and close to 0, which means the surface Y6 molecules are in a perfect face-on orientation. (c) Angle-dependent NEXAFS spectra of ITIC with 0.5% DIO before and after TA treatment. The ITIC film with 0.5% DIO after TA treatment shows a weaker angle-dependence. (d) Fitting plots of π* intensity *versus* $\sin^2(\theta)$.

 This journal is © The Royal Society of Chemistry 2023

Published on 08 May 2023. Downloaded by Xian Jiaotong University on 2/27/2026 2:24:49 AM.

the $B$ value would be TA-independent. It is worth noting that the absolute $B$ value of the ITIC film with 0.5% DIO before TA treatment is even larger than that of Y6 films with 0.5% CN, which means that the surface of the ITIC film with 0.5% DIO before TA treatment is extremely face-on oriented, confirming again the highly ordered property of the surface. Raman spectroscopy is employed to evidence the angle-dependent NEXAFS results, which is provided in Fig. S7 (ESI†). The intensity of the Raman shift is correlated with the orthogonality of the incident electric field and the functional group at the film surface. The reduced $\delta_{C=O}$ resonance signal of TA-treated ITIC indicates a partial decline in the surface ''face-on'' to ''edge-on'' orientation.

GIWAXS measurements are also carried out for the crystallinity characterization of PBDB-T:ITIC and PM6:Y6 films with additives (Fig. S8, ESI†). Although the X-ray incident angle is 0.12°, making the measurement bulk-sensitive, a significant decrease of the overall scattering of PBDB-T:ITIC after TA treatment is observed, as well as the loss of the fine structure, which means that the crystallinity of the whole film is decreased after TA treatment owing to Ostwald ripening. For PM6:Y6 blend films, the scattering is invariable after TA treatment, indicating a less crystalline change. The GIWAXS results agree with NEXAFS measurement.

### Surface energy level evaluation

We further performed the UPS and LEIPS measurements in the case of necessary surface energy level evaluation. UPS and LEIPS measurements can only be used to collect the secondary electrons from the surface (several nanometers) of the sample, so the UPS and LEIPS results actually characterize the property of the film surface.[50–52]

The summarized surface energy level parameters of ITIC and Y6 films with different treatments (with or without additives; with or without TA) are listed in Table 1, and the UPS and the LEIPS profiles of ITIC and Y6 neat films with different treatments are provided in Fig. S9 and S10 (ESI†), respectively. In the HOMO region, the four ITIC neat films are nearly the same, and the $E_{onset}$ values extracted from the plots are 1.73 ± 0.03 eV, 1.65 ± 0.03 eV, 1.86 ± 0.03 eV and 1.54 ± 0.03 eV for films of 0% DIO, 0% DIO + TA, 0.5% DIO and 0.5% DIO + TA, respectively. For the Y6 films, the $E_{onset}$ values are 2.32 ± 0.03 eV, 2.40 ± 0.03 eV, 1.76 ± 0.03 eV and 1.56 ± 0.03 eV for films of 0% CN, 0% CN + TA, 0.5% CN and 0.5% CN + TA, respectively, showing an additive-dependent shift. As for the secondary electron cutoff region, the binding energy of the ITIC film with 0.5% DIO addition is obviously shifted to higher binding energy with an $E_{cutoff}$ of 17.87 ± 0.03 eV, which is 1.13 eV higher than that after TA treatment (16.74 ± 0.03 eV). The $E_{cutoff}$ values of 0% DIO addition devices are 17.32 ± 0.03 eV and 17.08 ± 0.03 eV before and after TA treatment, respectively. For the Y6 films, the $E_{cutoff}$ values are 18.12 ± 0.03 eV, 18.26 ± 0.03 eV, 17.67 ± 0.03 eV and 17.28 ± 0.03 eV for films of 0% CN, 0% CN + TA, 0.5% CN and 0.5% CN + TA, respectively, which also show the additive-dependent shift.

The HOMO energy levels of the film surfaces can be extracted from UPS profiles using the following equation:

$$E_{HOMO} = 21.22 - (E_{cutoff} - E_{onset}) \quad (4)$$

where 21.22 is the energy of He I radiation, and $E_{cutoff}$ and $E_{onset}$ can be extracted from UPS plots. Thus the $E_{HOMO}$ of ITIC with 0% DIO, 0% DIO + TA, 0.5% DIO and 0.5% DIO + TA are −5.61 ± 0.06 eV, −5.77 ± 0.06 eV, −5.19 ± 0.06 eV and −6.00 ± 0.06 eV, respectively. For Y6 films, the $E_{HOMO}$ values are −5.42 ± 0.03 eV, −5.36 ± 0.03 eV, −5.31 ± 0.03 eV and −5.50 ± 0.03 eV for films of 0% CN, 0% CN + TA, 0.5% CN and 0.5% CN + TA, respectively. The optical band gap ($E_g$) can be calculated from UV-vis absorption spectra, which are plotted in Fig. 1(b) (PBDB-T and PM6 do not absorb in the region of 700–1000 nm). The calculated optical $E_g$ values of ITIC with 0% DIO, 0% DIO + TA, 0.5% DIO and 0.5% DIO + TA are 1.65 ± 0.03 eV, 1.64 ± 0.03 eV, 1.61 ± 0.03 eV and 1.63 ± 0.03 eV, respectively, thus the corresponding LUMO energy levels are −3.96 ± 0.06 eV, −4.13 ± 0.06 eV, −3.58 ± 0.06 eV and −4.37 ± 0.06 eV, which are obtained using the equation $E_{LUMO} = E_{HOMO} + E_g$.[53–56] For Y6 films, the optical $E_g$ values of 0% CN, 0% CN + TA, 0.5% CN and 0.5% CN + TA are 1.46 ± 0.03 eV, 1.45 ± 0.03 eV, 1.43 ± 0.03 eV and 1.42 ± 0.03 eV, respectively, thus the corresponding LUMO energy levels are −3.96 ± 0.06 eV, −3.91 ± 0.06 eV, −3.88 ± 0.06 eV and −4.08 ± 0.06 eV.

From LEIPS results (Fig. S10, ESI†), the surface LUMO energy levels of ITIC with 0.5% DIO before and after TA treatment can be obtained as −3.62 ± 0.03 eV and −4.03 ± 0.03 eV, respectively, while the surface LUMO energy levels of Y6 with 0.5% CN before and after TA treatment are −3.91 ± 0.03 eV and −3.95 ± 0.03 eV, respectively. The LEIPS results matched the UPS measurements and the optical band gap calculations.

In Fig. 5(a) and (b), the energy levels of PBDB-T, ITIC, PM6, and Y6 (CV method, from the literature[9,57]) and the surface energy levels of the ITIC and Y6 films with different treatments

Table 1 Summarized surface energy level parameters of ITIC and Y6 films with different treatments

| Materials | Treatment | $HOMO/LUMO_{CV}$ (eV) | $E_{onset}$ (eV) | $E_{cut\text{-}off}$ (eV) | $HOMO_{UPS}$ (eV) | $LUMO_{LEIPS}$ (eV) | $E_g^{opt}$ (eV) | $LUMO_{opt}$ (eV) |
|---|---|---|---|---|---|---|---|---|
| ITIC | 0% DIO | −5.61/−4.02 | 1.73 | 17.32 | −5.61 | — | 1.65 | −3.96 |
| | 0% DIO + 130 °C | | 1.65 | 17.08 | −5.77 | — | 1.64 | −4.13 |
| | 0.5% DIO | | 1.86 | 17.87 | −5.19 | −3.62 | 1.61 | −3.58 |
| | 0.5% DIO + 130 °C | | 1.54 | 16.74 | −6.00 | −4.03 | 1.63 | −4.37 |
| Y6 | 0% CN | −5.65/−4.10 | 2.32 | 18.12 | −5.42 | — | 1.46 | −3.96 |
| | 0% CN + 100 °C | | 2.40 | 18.26 | −5.36 | — | 1.45 | −3.91 |
| | 0.5% CN | | 1.76 | 17.67 | −5.31 | −3.91 | 1.43 | −3.88 |
| | 0.5% CN + 100 °C | | 1.56 | 17.28 | −5.50 | −3.95 | 1.42 | −4.08 |

Published on 08 May 2023. Downloaded by Xian Jiaotong University on 2/27/2026 2:24:49 AM.

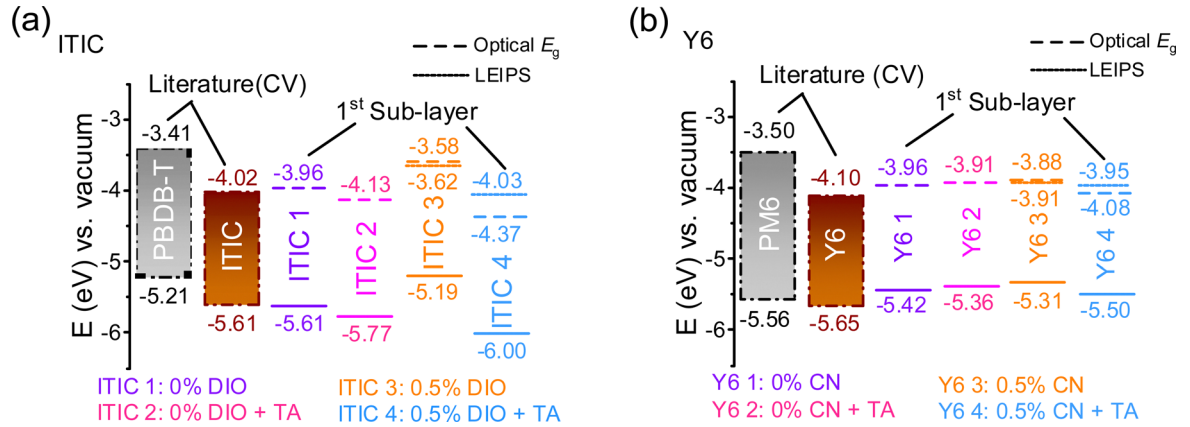



Fig. 5 Schematic diagram of energy levels (HOMO and LUMO). (a) The 1st sub-layers of ITIC films with different treatments. (b) The 1st sub-layers of Y6 films with different treatments. The energy levels of PBDB-T, PM6, ITIC and Y6 obtained from CV measurements are from the literature. The solid lines are HOMO energy levels obtained from UPS measurements. The dashed lines mean the LUMO energy levels which are calculated from the optical band gap, while the dotted lines represent the LUMO energy levels extracted from LEIPS measurements.

are displayed. As we can see, the energy levels of the surface of the ITIC film no. 3 (0.5% DIO) are quite close to that of PBDB-T, which is caused by a surface spinodal demixed highly ordered ITIC domain, and it is not beneficial for charge transport, resulting in poor exciton dissociation and carrier mobility on the surface which eventually acts as an "electron block layer". After TA treatment, the energy level of ITIC becomes deeper and the difference between the surface and PBDB-T becomes larger, which is caused by Ostwald ripening, benefiting exciton dissociation and charge transport. On the other hand, the energy level (LUMO especially) of the surface that comes into contact with the electrode is lower after TA treatment, fitting well with the reduced $V_{OC}$. For Y6 films, because of surface binodal demixing which is consistent with the film bulk, no significant energy level fluctuation is observed, indicating that the exciton dissociation and charge transport would not be influenced.

### Device performance characterization and charge dynamics

The *J*–*V* results of PBDB-T:ITIC and PM6:Y6 blend films are in accordance with expectations, as shown in Fig. 6(a) and the device performance parameters of PBDB-T:ITIC and PM6:Y6 blend films are summarized in Table 2. The PCEs of the as-cast device of PBDB-T:ITIC and PM6:Y6 are 9.5% and 14.4%, respectively, which are slightly lower than those of the devices after TA treatment of 9.8% and 15.1%, respectively. The $V_{OC}$ values become lower after TA treatment, which is related to the deeper energy level according to the UPS results, and the higher FF values of the devices after TA treatment are owing to the higher crystallinity. As for the PBDB-T:ITIC devices with 0.5% DIO addition, the TA-treated device with 0.5% DIO addition exhibits the best performance of $V_{OC}$, $J_{SC}$, FF and PCE of 0.913 V, 15.21 mA cm$^{-2}$, 0.733 and 10.2%, respectively. The FF and JSC values are significantly improved, compared with the device with 0.5% DIO before TA treatment (0.917 V, 14.49 mA cm$^{-2}$, 0.685 and 9.1%, respectively), which is mainly caused by the enhanced charge transport given by the degradation of the highly ordered surface layer. For the PM6:Y6 devices with 0.5% CN addition, the TA treatment only helps modify the crystal defects, thus the PCE is slightly improved from 16.0% to 16.4%. The EQE results are plotted in Fig. 6(b), and the calculated $J_{SC}$ values of all the devices are in agreement with the *J*–*V* results. The mobility measurement was carried out by the space charge limited current (SCLC) method and the results are provided in Fig. 6(c), and the corresponding *J*–*V* plots and fitting plots are provided in Fig. S11 (ESI†). It is shown that the TA treatment is able to improve both the hole and electron mobilities of PBDB-T:ITIC and PM6:Y6 blend films. For PBDB-T:ITIC blend films, DIO addition will largely reduce the electron mobility, leading to poor electron transport, and thus reduced $J_{SC}$ and FF values, which is caused by the surface energy level unmatched ITIC highly ordered domains. After TA treatment, the electron mobility is significantly enlarged with the hole mobility slightly improving, which contributes to higher $J_{SC}$ and FF values. However, for PM6:Y6 blend films, no obvious additive-dependence is exhibited, indicating that CN would not significantly influence the film crystallinity.

We further exchange the additives for PBDB-T:ITIC and PM6:Y6 devices. The device performances are characterized, and the *J*–*V* results are plotted in Fig. S12 (ESI†), and the summarized device parameters are listed in Table S2 (ESI†). The PBDB-T:ITIC devices with 0.5% CN additives after TA treatment exhibit less FF and PCE enhancement (from 0.676 to 0.702, and from 9.3% to 9.8%, respectively) than that with 0.5% DIO, while the PM6:Y6 devices with 0.5% DIO additives show almost the same enhancement after TA treatment as that of devices with 0.5% CN additives. These results matched with the corresponding FLAS results and the additives/acceptor liquid–solid transition diagrams, indicating that during solvent evaporation no spinodal demixed surface highly ordered acceptor layer is formed in both PBDB-T:ITIC and PM6:Y6 blend films.

In order to investigate the impact of additive and TA treatment on the degree of charge recombination processes, intensity ($P_{light}$) dependent photocurrent ($J_{SC}$) and $V_{OC}$ measurements have been performed. The relationship between $J_{SC}$ and $P_{light}$ follows a power-law: $J_{SC} \propto P_{light}^{\alpha}$, where $\alpha$ is close to unity,

 This journal is © The Royal Society of Chemistry 2023

Published on 08 May 2023. Downloaded by Xian Jiaotong University on 2/27/2026 2:24:49 AM.

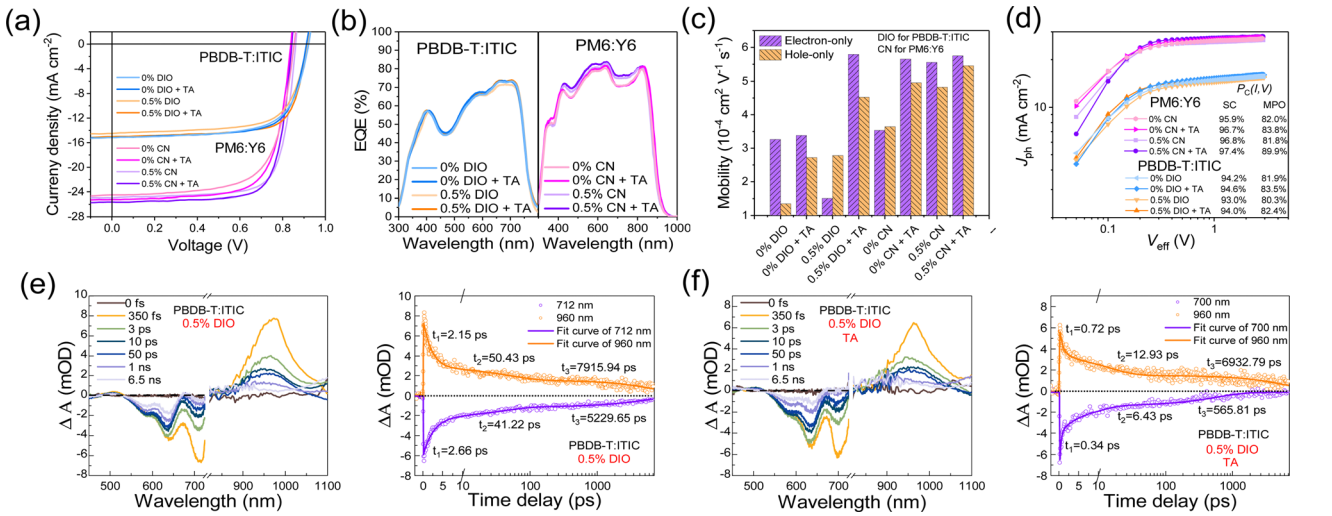



Fig. 6 Device performance characterization. (a) $J$–$V$ plots of PBDB-T:ITIC and PM6:Y6 blend films with different treatments. An obvious FF enhancement is shown in the PBDB-T:ITIC device after TA treatment, while no significant change is observed in the PM6:Y6 device after TA treatment. (b) EQE profiles of PBDB-T:ITIC and PM6:Y6 blend films with different treatments. (c) Mobilities of electron-only and hole-only devices of PBDB-T:ITIC and PM6:Y6 blend films with different treatments. (d) The $J_{ph}$–$V_{eff}$ curves of PBDB-T:ITIC and PM6:Y6 blend films with different treatments. The fs-TA spectra of the PBDB-T:ITIC blend film with 0.5% DIO (e) before and (f) after TA treatment. Kinetic studies: at 712/700 nm and 960 nm.

Table 2 Summarized device performance parameters of PBDB-T:ITIC and PM6:Y6 blend films with or without additives before or after TA treatment

| Device | Treatment | $V_{OC}$ (V) | $J_{SC}$ (mA cm$^{-2}$) | $J_{SC}^{EQE}$ (mA cm$^{-2}$) | FF | PCE[a] (%) |
|---|---|---|---|---|---|---|
| PBDB-T/ITIC | 0% DIO | 0.922 | 15.17 | 15.10 | 0.680 | 9.5 (9.3 ± 0.1) |
| PBDB-T/ITIC | 0% DIO + 130 °C | 0.910 | 15.34 | 15.25 | 0.706 | 9.8 (9.6 ± 0.1) |
| PBDB-T/ITIC | 0.5% DIO | 0.917 | 14.49 | 14.82 | 0.685 | 9.1 (8.9 ± 0.2) |
| PBDB-T/ITIC | 0.5% DIO + 130 °C | 0.913 | 15.21 | 15.26 | 0.733 | 10.2 (9.9 ± 0.1) |
| PM6/Y6 | 0% CN | 0.849 | 24.56 | 23.83 | 0.689 | 14.4 (14.2 ± 0.2) |
| PM6/Y6 | 0% CN + 100 °C | 0.838 | 25.22 | 24.31 | 0.713 | 15.1 (14.8 ± 0.2) |
| PM6/Y6 | 0.5% CN | 0.861 | 24.84 | 24.41 | 0.747 | 16.0 (15.7 ± 0.2) |
| PM6/Y6 | 0.5% CN + 100 °C | 0.842 | 25.58 | 25.17 | 0.763 | 16.4 (16.1 ± 0.2) |

[a] All average values with standard deviations were calculated from 10 devices.

suggesting minimal bimolecular recombination.[10] As shown in Fig. S13a (ESI†), the TA treatment and additives are able to help reduce the bimolecular recombination in both PBDB-T:ITIC and PM6:Y6 films. The degree of trap-assisted recombination in devices can be determined by the slope of $V_{OC}$ *versus* $\ln P_{light}$, as provided in Fig. S13b (ESI†). The slope is close to $kT/q$, where $k$ is Boltzmann's constant, $T$ is the absolute temperature and $q$ is the elementary charge, suggesting a bimolecular recombination system, while the slope is close to $2kT/q$ suggesting a trap-assisted recombination system. Enhanced $V_{OC}$ dependence on $P_{light}$ means a higher trap-assisted recombination ratio. A conclusion can be drawn from Fig. S13 (ESI†) that additives can significantly aggravate trap-assisted recombination while TA treatment is able to refine the traps inside the films. The increased trap-assisted recombination after DIO/CN addition may be caused by the increased trap state density arising from the numerous crystal boundaries.

The photocurrent density ($J_{ph}$) as a function of the effective voltage ($V_{eff}$) was afterwards measured to obtain more insights into exciton dissociation and charge collection, and the results are shown in Fig. 6(d). $J_{ph}$ is determined by $J_{ph} = J_L - J_D$, where $J_L$ is the photocurrent density under illumination, and $J_D$ is the photocurrent density in the dark.[12] $V_{eff}$ is calculated by $V_{eff} = V_0 - V_a$, where $V_0$ is the voltage at $J_{ph} = 0$ and $V_a$ is the applied voltage. Assuming that all the charges are dissociated into free carriers and collected by the electrodes under saturated current conditions ($V_{eff} > 3$ V), the charge collection probability $P_C(I,V)$,[58] where $I$ is the light intensity and $V$ is the applied voltage, can be determined by normalizing $J_{ph}$ with $J_{sat}$, where $J_{sat}$ is the saturation $J_{ph}$. For PM6:Y6 with 0.5% CN after TA treatment, the simultaneous enhancement $P_C(I,V)$ under both short-circuit (SC) and maximum power output (MPO) conditions results (97.4% and 89.9%) in the highest $J_{SC}$ and FF. For the PBDB-T:ITIC system, the film with 0.5% DIO before TA treatment exhibits the poorest $P_C(I,V)$ results under both SC and MPO conditions (93.0% and 80.3%), leading to the lowest $J_{SC}$ and FF, which is caused by the unbalanced charge carrier mobility and the high charge recombination probability, as a result of the energy level unmatched surface layer.

The photophysical process of PBDB-T:ITIC blend films with additives before and after TA treatment is investigated by femtosecond time-resolved transient absorption (fs-TA) spectroscopy,[59] as shown in Fig. 6(e) and (f), and the 2D plots

Published on 08 May 2023. Downloaded by Xian Jiaotong University on 2/27/2026 2:24:49 AM.

are provided in Fig. S14 (ESI†). The blend films are excited at 770 nm to achieve ITIC selected excitation. The PBDB-T:ITIC films show clear ground state bleaching (GSB) signals in the range of 550–750 nm (550–670 nm for PBDB-T and 670–720 nm for ITIC), which indicates electron transitions from the ground state to an excited state. The excited-state absorption (ESA) of PBDB-T:ITIC blends, which is usually in the form of singlet excitons,[60] is located in the range of 900–1050. It is noted that the polaron/CT-state absorption of organic semiconductors is usually located in the range of 1200–1600 nm,[61–63] which is out of the measurement limit of our fs-TA equipment. The GSB signals of ITIC rise to the maximum in 350 fs, indicating the ultrafast exciton formation process, and the GSB signals of PBDB-T rise followed by that of ITIC, which indicates the efficient charge transfer from the acceptors to the donors. Using the multiexponential decay function, these characteristic peaks were fitted to reveal the ultrafast kinetics of TA spectra. The GSB signals of ITIC with 0.5% DIO before TA treatment probed at 712 nm exhibit three recovery processes with $t_1$ =2.66 ps, $t_2$ = 41.22 ps, and $t_3$ = 5229.65 ps, while those lifetimes of the film after TA treatment (700 nm) are 0.34 ps, 6.43 ps and 565.81 ps. The three lifetimes approximately represent three physical processes: $t_1$ for exciton relaxation *via* internal conversion, vibrational relaxation and structural relaxation ($\sim$1 ps),[63] because this time-scale is much smaller than that of hole transfer ($\sim$10 ps) which is attributed to the $t_2$ component,[64] and $t_3$ for a long-lived component such as triplet state excitons.[65] The ESA lifetime can be also extracted from ESA signals by using the multiexponential decay function. The fitted ESA results for PBDB-T:ITIC with 0.5% DIO before TA treatment probed at 960 nm showed three processes with $t_1$ = 2.15 ps, $t_2$ = 50.43 ps and $t_3$ = 7915.94 ps, which could be tentatively attributed to the transition of excitons in an excited state ($\sim$1 ps),[63] the charge transfer from the acceptors to the donors ($\sim$10–50 ps),[60] and the slower polaron formation and/or exciton decay,[60,66,67] respectively. The ESA time constants of PBDB-T:ITIC with 0.5% DIO after TA treatment ($t_1$ = 0.72 ps, $t_2$ = 12.93 ps and $t_3$ = 6932.79 ps) are also much smaller than those before TA treatment. These results suggest that the excitons decay of the film after TA treatment is significantly faster than that before TA treatment, showing a higher exciton dissociation rate. The reduced EQE of the device before TA treatment in the range of 600–730 nm is also attributed to the poor exciton dissociation efficiency analyzed from the fs-TA measurements.[68,69]

The fs-TA spectra results of PM6:Y6 are provided in Fig. S15 (ESI†), which shows a similar rule to PBDB-T:ITIC films, indicating that both PBDB-T:ITIC and PM6:Y6 experienced similar physical processes after being excited.

Since PBDB-T:ITIC films with 0.5% DIO addition exhibit unusual properties, we further investigated the effects of TA time and TA temperature on the absorption spectrum of the 1st sub-layer of the PBDB-T:ITIC blend films, and compared the absorption spectrum of the 1st sub-layer with the device performances, as shown in Fig. S16 (ESI†). Only the wavelength of maximum absorption of the 1st sub-layer significantly varies with the increased TA temperature and TA time, which means that the other layers should be less influential, so the impact on device performance should be small. With the increase of TA temperature (for 5 min) and TA time (at 70 °C for slower evolution), the FF value gradually increases with the blue shift of the absorption peak of the 1st sub-layer, while the $V_{OC}$ value decreases, indicating that the increased charge transfer is owing to the energy level sinking of the 1st sub-layer after TA treatment.

During the investigation, we found that ITIC derivatives also feature a highly ordered surface layer, and the role of TA treatment is also the same. We take some of them as examples with their *J*–*V* results plotted in Fig. S17 (ESI†) and their OSC performance parameters are provided in Table S3 (ESI†). ITIC derivative-based devices include PBDB-T:ITCC, PBDB-T:ITTC and PBDB-T:IT-4Cl, and the absorption peaks of acceptors are blue-shifted after TA treatment, which means a highly ordered surface layer is formed after 0.5% DIO addition, and then the crystallinity of this layer is decreased after TA treatment. The devices of ITIC derivatives will be more efficient after TA treatment. The PCEs of TA-treated devices of PBDB-T:ITCC, PBDB-T:ITTC and PM6:IT-4Cl blend films are 9.2%, 8.2% and 13.6%, respectively, which are obviously higher than those before TA-treated devices of 7.5%, 7.2% and 12.9%. The remarkable increase of FF values from 0.596 to 0.685, 0.614 to 0.656, and 0.712 to 0.736, respectively, for PBDB-T:ITCC, PBDB-T:ITTC and PM6:IT-4Cl blend films is due to the degradation of their highly ordered surface layer.

## Conclusions

In summary, a highly ordered surface in the PBDB-T:ITIC blend film deposited from solution with 0.5% DIO is found by the FLAS technique. However, this highly-ordered layer is not present in PM6:Y6 blend films with 0.5% CN. This layer is formed through spinodal demixing of ITIC and DIO at the solvent free surface, which is proved by the Flory–Huggins interaction parameters, while the surface of PM6:Y6 is demixed through a binodal path. After TA treatment, the film crystallinity is decreased owing to the Ostwald ripening; meanwhile, the surface LUMO energy level of ITIC is dropped by 0.81 eV, matching that of PBDB-T. The PCE of the PBDB-T:ITIC blend film with 0.5% DIO additives is improved from 8.9 $\pm$ 0.2% (before TA) to 9.9 $\pm$ 0.1% (after TA), with remarkably improved FF values from 0.685 to 0.733. For PM6:Y6 blend films, such a highly ordered surface and energy level fluctuation along the film-depth direction do not exist, so TA treatment does not significantly lead to device performance enhancement (15.7 $\pm$ 0.2% to 16.1 $\pm$ 0.2%). The summarized device performances of both PBDB-T:ITIC with different TA conditions and other materials (ITIC derivatives) are strongly correlated with the absorption peak locations of the 1st sub-layer. This phenomenon verifies that surface phase segregation significantly determines the photovoltaic performance and may help improve the performances of OSCs and other organic electronics.

 This journal is © The Royal Society of Chemistry 2023

Published on 08 May 2023. Downloaded by Xian Jiaotong University on 2/27/2026 2:24:49 AM.

## Author contributions

This manuscript was written through contributions of all authors. All authors have given approval to the final version of the manuscript.

## Conflicts of interest

There are no conflicts to declare.

## Acknowledgements

This work was financially funded by the National Natural Science Foundation of China (grants no. 51873172, 21973072, 52273026 and 51907148) and the Youth Fund of State Key Laboratory of Electrical Insulation and Power Equipment (EIPE23407). G. L. thanks the Key Scientific and Technological Innovation Team Project of Shaanxi Province (2021GXLH-Z-055). The authors thank the Shanghai Synchrotron Radiation Facility (SSRF) for providing GIWAXS measurement. The authors also thank the Catalysis and Surface Science Endstation at the BL11U beamline in the National Synchrotron Radiation Laboratory (NSRL) for help with the characterization.

## References

1 L. Meng, Y. Zhang, X. Wan, C. Li, X. Zhang, Y. Wang, X. Ke, Z. Xiao, L. Ding, R. Xia, H.-L. Yip, Y. Cao and Y. Chen., *Science*, 2018, **361**, 1094–1098.
2 A. J. Gillett, A. Privitera, R. Dilmurat, A. Karki, D. Qian, A. Pershin, G. Londi, W. K. Myers, J. Lee, J. Yuan, S. J. Ko, M. K. Riede, F. Gao, G. C. Bazan, A. Rao, T. Q. Nguyen, D. Beljonne and R. H. Friend, *Nature*, 2021, **597**, 666–671.
3 Y. Zhu, Y. Fan, S. Li, P. Wei, D. Li, B. Liu, D. Cui, Z. Zhang, G. Li, Y. Niee and G. Lu., *Mater. Horiz.*, 2020, **7**, 1861.
4 H. W. Cheng, Y. Zhao and Y. Yang, *Adv. Energy Mater.*, 2021, **12**, 2102908.
5 S. Guo, Y. Hu, M. Qin, J. Li, Y. Wang, J. Qin and P. Cheng, *Mater. Horiz.*, 2022, **9**, 2097–2108.
6 J. Zhang, H. S. Tan, X. Guo, A. Facchetti and H. Yan, *Nat. Energy*, 2018, **3**, 720–731.
7 L. Zhu, M. Zhang, W. Zhong, S. Leng, G. Zhou, Y. Zou, X. Su, H. Ding, P. Gu, F. Liu and Y. Zhang, *Energy Environ. Sci.*, 2021, **14**, 4341–4357.
8 Q. Li, Y. Sun, X. Xue, S. Yue, K. Liu, M. Azam, C. Yang, Z. Wang, F. Tan and Y. Chen, *ACS Appl. Mater. Interfaces*, 2019, **11**, 3299–3307.
9 L. Nian, Y. Kan, H. Wang, K. Gao, B. Xu, Q. Rong, R. Wang, J. Wang, F. Liu, J. Chen, G. Zhou, T. P. Russell and A. K. Y. Jen, *Energy Environ. Sci.*, 2018, **11**, 3392–3399.
10 W. Feng, S. Wu, H. Chen, L. Meng, F. Huang, H. Liang, J. Zhang, Z. Wei, X. Wan, C. Li, Z. Yao and Y. Chen, *Adv. Energy Mater.*, 2022, **12**, 2104060.
11 L. Guo, Q. Li, J. Ren, Y. Xu, J. Zhang, K. Zhang, Y. Cai, S. Liu and F. Huang, *Energy Environ. Sci.*, 2022, **15**, 5137.
12 J. Qin, Q. Yang, J. Oh, S. Chen, G. O. Odunmbaku, N. A. N. Ouedraogo, C. Yang, K. Sun and S. Lu, *Adv. Sci.*, 2022, **9**, e2105347.
13 H. Tan, B. Yuan, Z. Shao, W. Deng, J. Yu, M. Xiao, H. Wu and W. Zhu, *Chem. Eng. J.*, 2022, **445**, 136691.
14 H.-C. Liao, C.-C. Ho, C.-Y. Chang, M.-H. Jao, S. B. Darling and W.-F. Su, *Mater. Today*, 2013, **16**, 326–336.
15 F. Machui, P. Maisch, I. Burgues-Ceballos, S. Langner, J. Krantz, T. Ameri and C. J. Brabec, *ChemPhysChem*, 2015, **16**, 1275–1280.
16 C. McDowell, M. Abdelsamie, M. F. Toney and G. C. Bazan, *Adv. Mater.*, 2018, **30**, 1707114.
17 O. Alqahtani, J. Lv, T. Xu, V. Murcia, T. Ferron, T. McAfee, D. Grabner, T. Duan and B. A. Collins, *Small*, 2022, **18**, e2202411.
18 J. Fu, H. Chen, P. Huang, Q. Yu, H. Tang, S. Chen, S. Jung, K. Sun, C. Yang, S. Lu, Z. Kan, Z. Xiao and G. Li, *Nano Energy*, 2021, **84**, 105862.
19 K. E. Hung, Y. S. Lin, Y. J. Xue, H. R. Yang, Y. Y. Lai, J. W. Chang, C. J. Su, A. C. Su, C. S. Hsu, U. S. Jeng and Y. J. Cheng, *Adv. Energy Mater.*, 2022, **12**, 2103702.
20 E. Moustafa, A. A. A. Torimtubun, J. Pallarès and L. F. Marsal, *Sol. RRL*, 2021, **6**, 2100480.
21 H. N. Tran, D. H. Kim, S. Park and S. Cho, *Curr. Appl. Phys.*, 2018, **18**, 534–540.
22 S. Karuthedath, Y. Firdaus, A. D. Scaccabarozzi, M. I. Nugraha, S. Alam, T. D. Anthopoulos and F. Laquai, *Small Struct.*, 2022, **3**, 2100199.
23 X. Song, N. Gasparini and D. Baran, *Adv. Electron. Mater.*, 2018, **4**, 1700358.
24 S. Xie, J. Wang, R. Wang, D. Zhang, H. Zhou, Y. Zhang and D. Zhou, *Chin. Chem. Lett.*, 2019, **30**, 217–221.
25 L. Zhao, H. Ji, S. Li, Q. Shi, C. Zhu, W. Wang and D. Huang, *Appl. Surf. Sci.*, 2021, **569**, 151120.
26 Z. Zheng, E. He, J. Wang, Z. Qin, T. Niu, F. Guo, S. Gao, Z. Ma, L. Zhao, X. Lu, Q. Xue, Y. Cao, G. T. Mola and Y. Zhang, *J. Mater. Chem. A*, 2021, **9**, 26105–26112.
27 X. Li, R. Zhu, Z. He, X. Du, H. Lin, C. Zheng, G. Yang, Z. Chen and S. Tao, *ACS Appl. Mater. Interfaces*, 2022, **14**, 25842–25850.
28 Z. Xiao, Y. Yuan, B. Yang, J. VanDerslice, J. Chen, O. Dyck, G. Duscher and J. Huang, *Adv. Mater.*, 2014, **26**, 3068–3075.
29 L. Zhao, H. Ji, S. Li, X. Miao, Q. Shi, C. Zhu, W. Wang, S. Zhao, D. Huang and X. Dong, *Org. Electron.*, 2022, **105**, 106495.
30 J. Song, L. Zhu, C. Li, J. Xu, H. Wu, X. Zhang, Y. Zhang, Z. Tang, F. Liu and Y. Sun, *Matter.*, 2021, **4**, 2542–2552.
31 X. Wang, L. Zhang, L. Hu, Z. Xie, H. Mao, L. Tan, Y. Zhang and Y. Chen, *Adv. Funct. Mater.*, 2021, **31**, 2102291.
32 L. Bu, S. Gao, W. Wang, L. Zhou, S. Feng, X. Chen, D. Yu, S. Li and G. Lu, *Adv. Electron. Mater.*, 2016, **2**, 1600359.
33 S. He, Z. Shen, J. Yu, H. Guan, G. Lu, T. Xiao, S. Yang, Y. Zou and L. Bu, *Adv. Mater. Interfaces*, 2020, **7**, 2000577.
34 Z. Shen, Y. Jiang, J. Yu, Y. Zhu, L. Bu and G. Lu, *Adv. Mater. Interfaces*, 2021, **8**, 2101476.
35 Z. Wang, Y. Hu, T. Xiao, Y. Zhu, X. Chen, L. Bu, Y. Zhang, Z. Wei, B. B. Xu and G. Lu, *Adv. Opt. Mater.*, 2019, **7**, 1900152.

Published on 08 May 2023. Downloaded by Xian Jiaotong University on 2/27/2026 2:24:49 AM.

36 J. Yu, Y. Xing, Z. Shen, Y. Zhu, D. Neher, N. Koch and G. Lu, *Mater. Horiz.*, 2021, **8**, 1461–1471.
37 S. Liang, S. Li, Y. Zhang, T. Li, H. Zhou, F. Jin, C. Sheng, G. Ni, J. Yuan, W. Ma and H. Zhao, *Adv. Funct. Mater.*, 2021, **31**, 2102764.
38 Y. Yang, Z. G. Zhang, H. Bin, S. Chen, L. Gao, L. Xue, C. Yang and Y. Li, *J. Am. Chem. Soc.*, 2016, **138**, 15011–15018.
39 C. Zhai, X. Yang, S. Han, G. Lu, P. Wei, A. Chumakov, E. Erbes, Q. Chen, S. Techert, S. V. Roth, P. Zhang and L. Bu, *Chem. Mater.*, 2021, **33**, 2673–2682.
40 E. F. Manley, J. Strzalka, T. J. Fauvell, N. E. Jackson, M. J. Leonardi, N. D. Eastham, T. J. Marks and L. X. Chen, *Adv. Mater.*, 2017, **29**, 1703933.
41 D. Yang, S. Grott, X. Jiang, K. S. Wienhold, M. Schwartzkopf, S. V. Roth and P. Müller-Buschbaum, *Small Methods*, 2020, **4**, 2000418.
42 A. J. Patel and N. P. Balsara, *Macromolecules*, 2007, **40**, 1675–1683.
43 P. Zhang and Z.-G. Wang, *Macromolecules*, 2022, **55**, 3910–3923.
44 N. Li, J. D. Perea, T. Kassar, M. Richter, T. Heumueller, G. J. Matt, Y. Hou, N. S. Guldal, H. Chen, S. Chen, S. Langner, M. Berlinghof, T. Unruh and C. J. Brabec, *Nat. Commun.*, 2017, **8**, 14541.
45 J. Y. Kim, *Polymers*, 2021, **13**, 983.
46 Y. Li, H. Liu, J. Wu, H. Tang, H. Wang, Q. Yang, Y. Fu and Z. Xie, *ACS Appl. Mater. Interfaces*, 2021, **13**, 10239–10248.
47 G. Qu, K. S. Park, P. Kafle, F. Zhang, J. J. Kwok, B. B. Patel, D.-M. Smilgies, L. Thomsen, C. R. McNeill and Y. Diao, *Chem. Mater.*, 2020, **32**, 6043–6054.
48 J. Stöhr and M. G. Samant, *J. Electron Spectrosc. Relat. Phenom.*, 1999, **98–99**, 189–207.
49 S. N. Patel, G. M. Su, C. Luo, M. Wang, L. A. Perez, D. A. Fischer, D. Prendergast, G. C. Bazan, A. J. Heeger, M. L. Chabinyc and E. J. Kramer, *Macromolecules*, 2015, **48**, 6606–6616.
50 N.-W. Teng, C.-H. Li, W.-C. Lo, Y.-S. Tsai, C.-Y. Liao, Y.-W. You, H.-L. Ho, W.-L. Li, C.-C. Lee, W.-C. Lin and Y.-M. Chang, *Sol. RRL*, 2020, **4**, 2000223.
51 D. J. Yun, Y. Yun, J. Lee, J. Y. Kim, J. Chung, S. H. Kim, Y. S. Kim, S. Heo, J. I. Park, K. H. Kim, Y. N. Kwon and J. W. Chung, *ACS Appl. Mater. Interfaces*, 2020, **12**, 50628–50637.
52 H. Sato, S. A. A. Rahman, Y. Yamada, H. Ishii and H. Yoshida, *Nat. Mater.*, 2022, **21**, 910–916.
53 B. Zhang, Y. Luo, C. Mai, L. Mu, M. Li, J. Wang, W. Xu and J. Peng, *Nanomaterials*, 2021, **11**, 1246.
54 Y. Dang, G. Tong, W. Song, Z. Liu, L. Qiu, L. K. Ono and Y. Qi, *J. Mater. Chem. C*, 2020, **8**, 276.
55 R. Pandiyana, Z. O. Elhmaidi, Z. Sekkat, M. Abd-lefdil and M. A. E. Khakani, *Appl. Surf. Sci.*, 2017, **396**, 1562–1570.
56 S. B. A. Hamida, S. J. Teha, C. W. Lai, S. Perathoner and G. Centi, *J. Energy Chem.*, 2017, **26**, 302–308.
57 X. Li, S. Luo, H. Sun, H. H. Sung, H. Yu, T. Liu, Y. Xiao, F. Bai, M. Pan, X. Lu, I. D. Williams, X. Guo, Y. Li and H. Yan, *Energy Environ. Sci.*, 2021, **14**, 4555.
58 A. K. K. Kyaw, D. H. Wang, V. Gupta, W. L. Leong, L. Ke, G. C. Bazan and A. J. Heeger, *ACS Nano*, 2013, **7**, 4569–4577.
59 Z. Liang, J. Tong, H. Li, Y. Wang, N. Wang, J. Li, C. Yang and Y. Xia, *J. Mater. Chem. A*, 2019, **7**, 15841–15850.
60 S. Liang, S. Li, Y. Zhang, T. Li, H. Zhou, F. Jin, C. Sheng, G. Ni, J. Yuan, W. Ma and H. Zhao, *Adv. Funct. Mater.*, 2021, **31**, 2102764.
61 Y. Zhong, M. T. Trinh, R. Chen, G. E. Purdum, P. P. Khlyabich, M. Sezen, S. Oh, H. Zhu, B. Fowler, B. Zhang, W. Wang, C.-Y. Nam, M. Y. Sfeir, C. T. Black, M. L. Steigerwald, Y.-L. Loo, F. Ng, X.-Y. Zhu and C. Nuckolls, *Nat. Commun.*, 2015, **6**, 8242.
62 J. Qin, Z. Chen, P. Bi, Y. Yang, J. Zhang, Z. Huang, Z. Wei, C. An, H. Yao, X. Hao, T. Zhang, Y. Cui, L. Hong, C. Liu, Y. Zu, C. He and J. Hou, *Energy Environ. Sci.*, 2021, **14**, 5903.
63 N. Zarrabi, P. L. Burn, P. Meredith and P. E. Shaw, *J. Phys. Chem. Lett.*, 2016, **7**, 2640–2646.
64 A. Weu, R. Kumar, J. F. Butscher, V. Lami, F. Paulus, A. A. Bakulin and Y. Yaynzof, *Adv. Funct. Mater.*, 2020, **30**, 1907432.
65 L. Yan, Z. Liang, J. Si, P. Gong, Y. Wang, X. Liu, J. Tong, J. Li and X. Hou, *ACS Appl. Mater. Interfaces*, 2022, **14**, 6945–6957.
66 S. Holliday, R. S. Ashraf, A. Wadsworth, D. Baran, S. A. Yousaf, C. B. Nielsen, C. H. Tan, S. D. Dimitrov, Z. Shang, N. Gasparini, M. Alamoudi, F. Laquai, C. J. Brabec, A. Salleo, J. R. Durrant and I. McCulloch, *Nat. Commun.*, 2016, **7**, 11585.
67 L. Lv, J. Yu, X. Sui, J. Wu, X. Dong, G. Lu, X. Liu, A. Peng and H. Huang, *J. Mater. Chem. C*, 2019, **7**, 5739.
68 M. Azzouzi, N. P. Gallop, F. Eisner, J. Yan, X. Zheng, H. Cha, Q. He, Z. Fei, M. Heeney, A. A. Bakulin and J. Nelson, *Energy Environ. Sci.*, 2022, **15**, 1256.
69 E. Collado-Fregoso, S. N. Pugliese, M. Wojcik, J. Benduhn, E. Bar-Or, L. P. Toro, U. Hörmann, D. Spoltore, K. Vandewal, J. M. Hodgkiss and D. Neher, *J. Am. Chem. Soc.*, 2019, **141**, 2329–2341.

 This journal is © The Royal Society of Chemistry 2023